Multi-fault Diagnosis for Lithium-ion Battery Packs in Energy Storage Systems

Hanxiao Liu, Luan Zhang, Bin Duan, *Senior Member*, *IEEE*, and Liwei Li

***Abstract*—Battery energy storage systems bolster power grids' absorption capacity, however, battery safety issues remain a formidable challenge. Timely and precise fault diagnosis, coupled with early-stage fault warnings, is crucial. This study introduces an eigen decomposition-based multi-fault diagnosis approach for lithium-ion battery packs, enabling online diagnosis of short circuits, electrical connection faults, and voltage sensor malfunctions. By incorporating an interleaved measurement topology, precise fault type differentiation is achieved. Eigenvector matching analysis is employed to increase sensitivity to fault characteristics and enhance robustness. The interleaved topology can be seamlessly integrated using common voltage measurement solutions, eliminating the need for additional design complexities, while sensor number redundancy enhances fault tolerance of battery management systems (BMS). A cloud-side collaboration method is proposed, where the BMS functions as an edge device for specific data computations, while the parameters are fine-tuned by the server through big data analytics. This approach circumvents cumbersome server calculations, thereby curbing server cost escalation. The edge computing process is divided into two steps, with partial calculations often sufficient to evaluate battery safety, thus reducing the computational load on edge devices. Several battery tests are conducted, and the results confirm the method's capability, feasibility, and validity in early-stage fault diagnosis.**

***Index Terms*—Eigen decomposition, fault diagnosis, interleaved topology, lithium-ion battery.**

I. Introduction

In recent years, growing environmental pollution and energy scarcity have become major constraints on economic development [1]. New energy generation technologies offer a crucial solution to alleviate these challenges. Integration of energy storage systems (ESS) not only boosts the ability to absorb renewable energy but also paves the way for addressing concerns related to excessive carbon emissions, environmental degradation, and energy shortages [2], [3].

ESS can be classified into various types, including battery storage, pumped hydro storage, compressed air storage, and flywheel storage. Among them, battery energy storage systems (BESS) have emerged as the most prevalent ESS approach, owing to their wide applicability, flexible deployment options, and relatively low investment requirements. Lithium-ion batteries, known for their high-power density and long service life, are extensively utilized in BESS [4], [5]. However, safety concerns surround lithium-ion batteries are escalating, as early-stage battery faults, often difficult to detect, can lead to rapid degradation and substantially heighten the risk of thermal runaway if not promptly addressed [6], [7]. Hence, it is crucial to integrate effective early fault diagnosis and localization techniques into the battery management systems (BMS) [8], [9].

A. Literature Review

In lithium-ion battery systems (LIBS), three prevalent faults can occur: short circuits (SC) fault, electrical connection (EC) fault, and voltage sensor (VS) fault. A SC fault represents a particularly hazardous form of abuse, often associated with the growth of lithium dendrites inside the batteries. Such faults can degrade battery performance and generate excessive heat, making them a primary cause of thermal runaway [10], [11]. Electrical abuse often stems from harsh operating conditions and inaccurate battery state estimations [12]. An EC fault manifests as a weakened connection between batteries, typically resulting from surface oxidation, substandard assembly, or intense vibrations [13]. When EC faults occur, the equivalent resistance between adjacent batteries increases, impairing the dynamic performance of the battery system. Moreover, unreliable EC between batteries can produce sparks, posing risks to the battery system's insulation. A VS fault presents itself in two ways: significant measurement errors and data stagnation, which adversely affect the accurate acquisition of battery voltages, thereby undermining the proper implementation

Received: March 6, 2025
Accepted: September 17, 2025
Published Online: January 1, 2026
Hanxiao Liu, Luan Zhang, and Bin Duan are with the School of Control Science and Engineering, Shandong University, Jinan 250061, China (e-mail: hanxliu@mail.sdu.edu.cn; zhluan@mail.sdu.edu.cn; duanbin@sdu.edu.cn).
Liwei Li (corresponding author) is with the School of Computer Science and Technology, Shandong University, Qingdao 266237, China (e-mail: liliwei@sdu.edu.cn).
DOI: 10.23919/PCMP.2024.000385

of battery protection strategies [14], [15]. The reasons and hazards of SC, EC, and VS faults are summarized in Fig. 1.

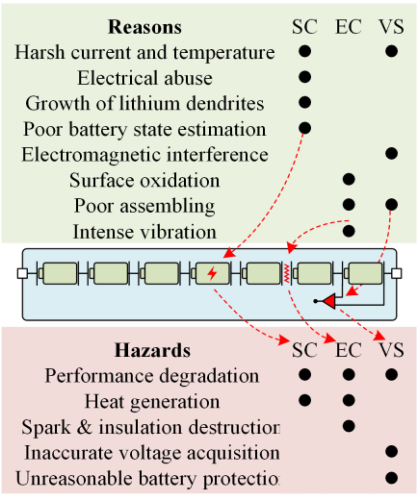

Fig. 1. Reasons and hazards of SC, EC, and VS faults.

Numerous scholars have carried out extensive research on fault diagnosis of lithium-ion batteries. Regarding fault detection methods, reference [16] develops an H_∞ nonlinear observer to estimate the state of charge (SOC) and soft SC current, leveraging an augmented state-space battery model. Soft SC faults are detected by comparing the observer-estimated SOC with the SOC calculated through Coulomb counting. Reference [17] introduces an aging-robust and disturbance-immune internal short circuit (ISC) diagnostic method for LIBs. This method integrates a multi-state-fusion ISC resistance estimator and an recursive total least squares with variant forgetting (RTLSVF)-based bias compensator within a unified model-switching framework. Reference [18] proposes a local gravitation outlier detection method for diagnosing faults in series-connected lithium-ion batteries. This approach can detect early-stage ISC faults using voltage signals, independent of battery models, even when fault characteristics are not obvious. In general, severely aged batteries are more prone to ISC faults, prompting many researchers to enhance the accuracy of state of health (SOH) estimation to more precisely quantify battery ageing. Reference [19] introduces a SOH estimation method grounded in the convolutional neural network-multi-gate mixture of gated recurrent units (CMMOG), which demonstrates faster learning convergence and superior generalization accuracy in experiments. Meanwhile, Reference [20] proposes a SOH estimation approach based on incremental energy per SOC and long short-term memory (LSTM)-reduction, exhibiting commendable effectiveness and robustness. However, both EC faults and VS faults cause discrepancies between the measured and actual battery terminal voltages, thereby compromising the accuracy of SOH estimation. Consequently, diagnosing EC and VS faults is crucial. Reference [21] develops a LSTM network to predict unmeasured current distributions using information readily available and calculable by the BMS, facilitating the diagnosis of EC faults. Reference [22] proposes an adaptive extended Kalman filter-based method for detecting and isolating sensor faults in lithium-ion battery packs, which adaptively adjusts measurement and process noise covariance. In [23], a hybrid system-based sensor fault diagnosis scheme is proposed for lithium-ion battery packs. It employs automata to model the battery pack and utilizes a dual extended Kalman filter algorithm for precise state and parameter estimation. Reference [24] utilizes an improved first-order equivalent battery model to validate current data against battery voltage data, enabling current sensor diagnostics. Reference [25] achieves multi-sensor fault diagnosis by extracting time-series features alongside three discriminative features, while reference [26] designs a set-valued diagnosis mechanism for detecting, identifying, and estimating faults in battery voltage and current sensors.

The primary challenge in distinguishing between fault types stems from the similarity in features among various faults. Furthermore, the subtlety of incipient fault indicators and the strong background noise generated by current-induced voltage fluctuations further complicate fault identification. Specifically, the flowing current induces a voltage drop across the battery's internal resistance, thereby altering the voltage measurement captured by sensors. Generally, a higher discharge current results in a lower measured voltage, while a higher charge current leads to a higher measured voltage, irrespective of other influencing factors. Similarly, EC faults increase the equivalent connection resistance between adjacent batteries, affecting the overall voltage measured by sensors in a manner akin to current variation. When an EC fault occurs, the affected battery establishes a separate discharge path, causing its voltage to gradually decline. During battery discharge, this phenomenon influences the measured voltage in a manner comparable to an EC fault. Conversely, a VS fault disrupts the data source for fault diagnosis methods, potentially leading to misdiagnosis of SC and EC faults due to the absence of effective fault type differentiation techniques. The impacts of different battery fault types are illustrated in Fig. 2, where V_{M} represents the measured voltage; i denotes the battery current; E signifies the battery electrochemical potential; R_{T} is the battery internal resistance, with u_{T} as its voltage; R_1 is the SC resistance; i_1 indicates the SC current; R_2 stands for the equivalent connection resistance between adjacent batteries and u_2 is its voltage.

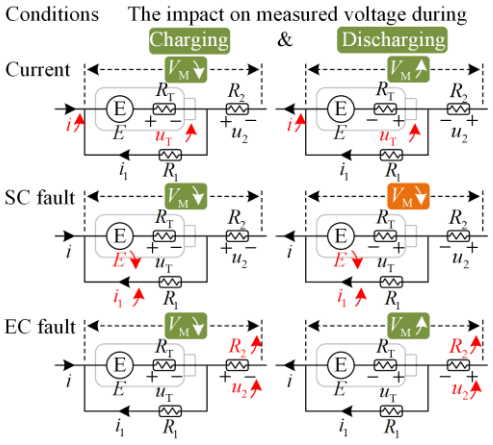

Fig. 2. The impact on battery voltage due to the current and faults.

To differentiate between battery fault types, various approaches have been explored. Reference [27] introduces a multi-fault diagnosis method for electric vehicle (EV) battery systems, leveraging curvilinear Manhattan distance evaluation and voltage difference analysis. This method quantifies the charging voltage variation curve to detect battery faults and employs a voltage difference analysis approach to pinpoint the specific faulty type. Reference [28] proposes a hybrid system mode estimation and discrete event system diagnosis method based on the Unscented Particle Filter at the module level to distinguish and diagnose battery cell parametric faults from sensor faults at the cell level. Accounting for the impact of inconsistencies in SOC and resistance on correlation coefficients, reference [29] develops a multi-fault diagnosis method using voltage difference correlation coefficients and variations to detect and isolate SC, VS, and EC faults, enhancing both diagnostic speed and accuracy. Reference [30] presents a vehicle-cloud coordinated multi-type fault diagnostics approach, achieving a 100% accuracy rate in detecting and isolating conventional faults of LIBSs, whereas reference [31] proposes an optimal sensor placement strategy aimed at detecting and isolating SC, EC, and VS faults within lithium-ion battery packs.

B. Motivations and Contributions

Multiple multi-fault diagnosis methods have been proposed to identify and pinpoint these three prevalent electrical faults in batteries. However, three key problems persist:

1) Different types of faults induce similar change patterns in battery data, making it challenging to distinguish between multiple faults accurately;

2) Early-stage fault features are extremely subtle and can easily be masked by substantial background noise, leading to a high misdiagnosis rate and making early fault diagnosis challenging [32];

3) BESS have large-scale battery systems, and conventional BMS are unable to handle the operation of advanced fault diagnosis methods. Continuously running these methods on cloud servers increases costs and suffers from limited real-time responsiveness.

To address the aforementioned challenges, this paper introduces a novel multi-fault diagnosis and localization approach. The key contributions are outlined as follows.

1) An eigen decomposition-based battery fault diagnosis method is proposed to diagnose the SC, EC, and VS faults. This approach is divided into two steps, where partial calculations are often adequate for assessing battery safety status in most cases, thereby reducing overall computational demands. Eigenvector matching analysis is employed to enhance sensitivity to fault characteristics and improve robustness.

2) The interleaved measurement topology is introduced to directly distinguish fault types, which can be readily implemented using standard battery sensors without additional design complexities.

3) A cloud-edge collaboration framework is proposed. Edge devices utilize optimized measurement and analysis (OPMA) techniques to distribute computational tasks among slave modules of the BMSs, effectively capping the maximum computational load. Meanwhile, cloud servers periodically upgrade algorithm parameters with minimal communication overhead.

The structure of the rest of the paper is outlined as follows. Section II details the interleaved measurement topology, the eigen-decomposition-based fault diagnosis method, and relevant optimization strategies. Section III presents the development of the battery experimental platform, while Section IV analyzes the experimental results and evaluates the method's performance. Finally, Section V draws the conclusions.

II. Topology and Fault Diagnosis Method

A. Interleaved Voltage Measurement Topology

In this study, the proposed approach employs an interleaved voltage measurement topology for battery voltage assessment and fault signature collection, as depicted in Fig. 3. In this topology, each sensor is tasked with measuring the voltage across one battery cell and one connecting resistor, i.e., every battery cell and connecting resistor are monitored by two sensors. Thus, the battery voltage can be accurately determined by averaging the two neighboring sensor values.

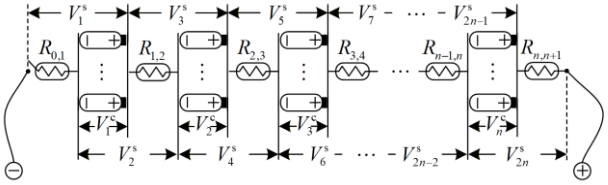

Fig. 3. Interleaved voltage measurement topology.

According to the circuit principle, the measured

voltage vector $\boldsymbol{V}^{\mathrm{s}}$ can be decomposed as:

$$\begin{bmatrix} V_1^{\mathrm{s}} \\ V_2^{\mathrm{s}} \\ \vdots \\ V_{2n}^{\mathrm{s}} \end{bmatrix} = \begin{bmatrix} 1 & 0 & \cdots & 0 \\ 1 & 0 & \cdots & 0 \\ 0 & 1 & \cdots & 0 \\ 0 & 1 & \cdots & 0 \\ \vdots & \vdots & & \vdots \\ 0 & 0 & \cdots & 1 \end{bmatrix} \begin{bmatrix} V_1^{\mathrm{c}} \\ V_2^{\mathrm{c}} \\ \vdots \\ V_{2n}^{\mathrm{c}} \end{bmatrix} - I \begin{bmatrix} 1 & 0 & \cdots & 0 & 0 \\ 0 & 1 & \cdots & 0 & 0 \\ 0 & 1 & \cdots & 0 & 0 \\ \vdots & \vdots & & \vdots & \vdots \\ 0 & 0 & \cdots & 1 & 0 \\ 0 & 0 & \cdots & 1 & 0 \\ 0 & 0 & \cdots & 0 & 1 \end{bmatrix} \begin{bmatrix} R_{0,1} \\ R_{1,2} \\ \vdots \\ R_{n-1,n} \\ R_{n,n+1} \end{bmatrix} \tag{1}$$

where V_i^{c} denotes voltage of the ith cell, which is measured by the $(2i)$th and $(2i-1)$th sensors; I represents the current of the battery pack; $R_{i,i+1}$ is the connection resistance between cell i and cell $i+1$, while $R_{0,1}$ and $R_{n,n+1}$ denote the negative and positive busbar connection resistances, respectively. Even though both the cell voltage V_i^{c} and battery current I are time-varying, the law of their changes is consistent.

Based on the topology, a VS fault affects only one element in $\boldsymbol{V}^{\mathrm{s}}$, while a SC fault and an EC fault affect two neighboring elements in $\boldsymbol{V}^{\mathrm{s}}$. Furthermore, drawing on (1), it is worth noting that, V_i^{c} is reflected in V_{2i-1}^{s} and V_{2i}^{s}, and is affected by SC faults; while $R_{i,i+1}$ is reflected in V_{2i}^{s} and V_{2i+1}^{s}, and is affected by EC faults. Thus, SC and EC faults can be further distinguished by the serial number of fault elements in the V_i^{s}.

For ease of analysis, it is assumed that there is only one fault in the entire battery system in the analysis, and this aligns well with the fault characteristics observed in most battery systems.

B. Fault Risk Indicator Eigenvalue Based Fault Detection Indicator

To devise an effective fault detection indicator, the eigenvalue analysis of covariance matrix for the streaming voltage data matrices is in-depth analyzed and deduced.

Without sacrificing generality, equation (1) can be reformulated as:

$$\boldsymbol{x} = \boldsymbol{A}\boldsymbol{s}_1 + \boldsymbol{B}\boldsymbol{s}_2 \tag{2}$$

where $\boldsymbol{x} \in \mathbb{R}^{2n\times 1}$ denotes the measurement voltage vector $\boldsymbol{V}^{\mathrm{s}}$; $\boldsymbol{A} \in \mathbb{R}^{2n\times n}$ represents the voltage coefficient matrix; $\boldsymbol{s}_1 \in \mathbb{R}^{n\times 1}$ denotes the cell voltage vector $\boldsymbol{V}^{\mathrm{c}}$; $\boldsymbol{B} \in \mathbb{R}^{2n\times(n+1)}$ signifies the link coefficient matrix; and $\boldsymbol{s}_2 \in \mathbb{R}^{(n+1)\times 1}$ is the voltage vector of n+1 connection resistances.

When extending along the time dimension, multiple samples of $\boldsymbol{x}$ within the time window w are collectively represented as $\boldsymbol{X}_k$, defined as follows:

$$\boldsymbol{X}_k = \begin{bmatrix} x_{k-w+1,1} & x_{k-w+1,2} & \cdots & x_{k-w+1,2n} \\ x_{k-w+2,1} & x_{k-w+2,2} & \cdots & x_{k-w+2,2n} \\ \vdots & \vdots & & \vdots \\ x_{k,1} & x_{k,2} & \cdots & x_{k,2n} \end{bmatrix} \tag{3}$$

Now, equation (2) is updated to:

$$\boldsymbol{X}_k = \boldsymbol{S}_{1,k}\boldsymbol{A}^{\mathrm{T}} + \boldsymbol{S}_{2,k}\boldsymbol{B}^{\mathrm{T}} \tag{4}$$

where $\boldsymbol{S}_{1,k} \in \mathbb{R}^{w\times n}$ and $\boldsymbol{S}_{2,k} \in \mathbb{R}^{w\times(n+1)}$.

Normalization is performed as follow:

$$\begin{aligned} \bar{\boldsymbol{X}}_k &= (\boldsymbol{X}_k - \boldsymbol{\mu}_0^{\mathrm{T}})\boldsymbol{\Sigma}_0^{-1} = \\ &(\boldsymbol{S}_{1,k}\bar{\boldsymbol{A}}^{\mathrm{T}} - \boldsymbol{\mu}_1^{\mathrm{T}}\boldsymbol{\Sigma}_0^{-1}) + (\boldsymbol{S}_{2,k}\bar{\boldsymbol{B}}^{\mathrm{T}} - \boldsymbol{\mu}_2^{\mathrm{T}}\boldsymbol{\Sigma}_0^{-1}) = \\ &\bar{\boldsymbol{S}}_{1,k}\bar{\boldsymbol{A}}^{\mathrm{T}} + \bar{\boldsymbol{S}}_{2,k}\bar{\boldsymbol{B}}^{\mathrm{T}} \end{aligned} \tag{5}$$

where $\boldsymbol{\mu}_0 = (\boldsymbol{\mu}_1 + \boldsymbol{\mu}_2) \in \mathbb{R}^{2n\times 1}$ is the mean value vector of $\boldsymbol{X}_k$, with $\boldsymbol{\mu}_1 = \boldsymbol{A}\boldsymbol{\mu}_{\mathrm{s}_1}$ and $\boldsymbol{\mu}_2 = \boldsymbol{B}\boldsymbol{\mu}_{\mathrm{s}_2}$ ($\boldsymbol{\mu}_{\mathrm{s}_1}$ and $\boldsymbol{\mu}_{\mathrm{s}_2}$ are the average vectors of $\boldsymbol{A}\boldsymbol{s}_1$ and $\boldsymbol{B}\boldsymbol{s}_2$ respectively); $\boldsymbol{\Sigma}_0 = \mathrm{diag}\left\{\sigma_{x_1}, \cdots, \sigma_{x_{2n}}\right\} \in \mathbb{R}^{2n}$ is the standard deviation diagonal-matrix of $\boldsymbol{X}_k$, which is obtained by analyzing the historical data; moreover, $\bar{\boldsymbol{A}} = (\boldsymbol{\Sigma}_0)^{-1}\boldsymbol{A}$ and $\bar{\boldsymbol{B}} = (\boldsymbol{\Sigma}_0)^{-1}\boldsymbol{B}$.

The decomposition of the $\boldsymbol{x}$ into $\boldsymbol{A}\boldsymbol{s}_1$ and $\boldsymbol{B}\boldsymbol{s}_2$ in (2) is to clarify what the $\boldsymbol{x}$ contains to start the subsequent analysis. At actual runtime, the only values that can be detected are the $\boldsymbol{x}$, and the detection as well as localization of battery faults is also based on the processing of the $\boldsymbol{x}$ without solving for $\boldsymbol{\mu}_{\mathrm{s}_1}$ and $\boldsymbol{\mu}_{\mathrm{s}_2}$.

The covariance matrix of $\bar{\boldsymbol{X}}_k$ can be expressed as:

$$\boldsymbol{C}_k = \boldsymbol{V}_k\boldsymbol{\Lambda}_k\boldsymbol{V}_k^{\mathrm{T}} \approx \frac{1}{w-1}\bar{\boldsymbol{X}}_k^{\mathrm{T}}\bar{\boldsymbol{X}}_k \tag{6}$$

where $\boldsymbol{\Lambda}_k = \mathrm{diag}\left\{\lambda_{1,k}, \lambda_{2,k}, \cdots, \lambda_{2n,k}\right\}$ is the eigenvalue diagonal matrix in descending order; while $\boldsymbol{V}_k$ represents the corresponding eigenvector matrix.

The high-order statistical characteristics of abnormal and normal states are orthogonal to each other. Consequently, abnormalities can be effectively characterized by eigenvalues that exclude contributions from normal component. To enhance the performance of the fault detection, we analyze the eigenvalue of the streaming matrices $\boldsymbol{X}_k$ in full-dimension and ultimately designed

the safety status indicator D_k drawing on the infinite norm of the eigenvalue $\lambda_{j,k}$ of $\boldsymbol{X}_k$, which can be formulated as:

$$D_k = \max_{1\leqslant j\leqslant 2n}\left|\lambda_{j,k}\right| = \left|\lambda_{1,k}\right| \tag{7}$$

where D_k represents the largest eigenvalue of the normalized covariance matrix derived from the measurement matrix within a given time window, serving as an indicator of the consistency in the changing patterns of vectors within the matrix. Upon the occurrence of a fault, the consistency between the measurements of the faulty component and the rest diminishes. In other words, the alignment of the changing trends among the different vectors within the measurement matrix weakens, causing a notable change in the eigenvalues of the covariance matrix, which in turn leads to a significant change in the D_k value.

1) In a fault-free battery pack, the voltage variations of individual batteries exhibit similar patterns. Specifically, battery voltage rises during charging, with higher charging currents corresponding to greater voltage increases; conversely, it drops during discharging, with higher discharge currents leading to more pronounced voltage decreases.

2) In the event of a SC fault, the affected battery's voltage exhibits distinct behavior from the others due to the SC current. Specifically, this battery experiences a more pronounced voltage drop during discharging and a less significant voltage rise during charging.

3) Similarly, when an EC fault arises between two adjacent batteries, their equivalent connection resistance increases, causing the corresponding sensor to register voltage variations that deviate from the norm. The VS measures a lower voltage during discharging and a higher voltage during charging.

4) If the sensor output value becomes unstable due to interference or other factors, the erratic portion of the output can cause the change rule of the faulty sensor's output value different with other sensors. Sensor data sticking represents the most severe manifestation of such faults, resulting in the faulty sensor's output displaying a completely different change rule.

C. Multi-fault Diagnosis Method

For convenience, it is assumed that only a single fault occurs within the entire battery system which aligns with the fault characteristics observed in most battery systems.

1) Detection Threshold for VS Fault

For a VS fault, the fault *f* at the *l*th channel x_l is denoted, and the measurement vector can be represented as:

$$\boldsymbol{x} = \boldsymbol{x}^* + \boldsymbol{\xi} f \tag{8}$$

where $\boldsymbol{x}^*$ denotes the fault-free part; $\boldsymbol{\xi} \in \mathbb{R}^{2n\times 1}$ signifies the fault weight, which is zero on fault-free channel and $\|\boldsymbol{\xi}\|_2 = 1$.

Denote $\bar{\boldsymbol{Y}}_k = \bar{\boldsymbol{S}}_{1,k}\bar{\boldsymbol{A}}^{\mathrm{T}} + \bar{\boldsymbol{S}}_{2,k}\bar{\boldsymbol{B}}^{\mathrm{T}}$ at time index *k*. Incorporating (5), the measurement vector within the time window *w* can be normalized as follows:

$$\bar{\boldsymbol{X}}_k = \bar{\boldsymbol{X}}_k^* + \boldsymbol{f}_k\boldsymbol{\xi}^{\mathrm{T}}\boldsymbol{\Sigma}_0^{-1} = \bar{\boldsymbol{Y}}_k + \boldsymbol{f}_k\boldsymbol{\xi}^{\mathrm{T}}\boldsymbol{\Sigma}_0^{-1} \tag{9}$$

where $\boldsymbol{f}_k \in \mathbb{R}^{w\times 1}$ signifies the fault vector at time index k in the fault duration *w*.

The covariance matrix $\boldsymbol{C}_k$ of $\bar{\boldsymbol{X}}_k$ can be classified into $\boldsymbol{C}_{1,k}$ and $\boldsymbol{C}_{2,k}$, which are formulated as follows:

$$\begin{cases} \boldsymbol{C}_{1,k} = w^{-1}\bar{\boldsymbol{Y}}_k^{\mathrm{T}}\bar{\boldsymbol{Y}}_k + w^{-1}\boldsymbol{\Sigma}_0^{-1}\boldsymbol{\xi}\boldsymbol{f}_k^{\mathrm{T}}\boldsymbol{f}_k\boldsymbol{\xi}^{\mathrm{T}}\boldsymbol{\Sigma}_0^{-1} \\ \boldsymbol{C}_{2,k} = w^{-1}\boldsymbol{\Sigma}_0^{-1}\boldsymbol{\xi}\boldsymbol{f}_k\bar{\boldsymbol{Y}}_k + w^{-1}\bar{\boldsymbol{Y}}_k^{\mathrm{T}}\boldsymbol{f}_k\boldsymbol{\xi}^{\mathrm{T}}\boldsymbol{\Sigma}_0^{-1} \end{cases} \tag{10}$$

The proposed fault detection indicator, as defined in (7), is directly linked to the eigenvalue distribution of the streaming covariance matrix $\boldsymbol{C}_k$. To further investigate the relationship between fault amplitude and the detection threshold, it is essential to derive the expected values of the eigenvalues.

According to rank-one modification theory for symmetric eigenvalue diagonal matrix [33], the eigenvalues $\bar{\lambda}_{j,k}\left(j = 1, 2, \cdots, 2n\right)$ satisfy:

$$\begin{cases} f(\bar{\lambda}_{j,k}) = 1 + \dfrac{\bar{\boldsymbol{f}}_k^{\mathrm{T}}\bar{\boldsymbol{f}}_k}{w}\sum_{i=1}^{2n}\dfrac{u_i^2}{\bar{\lambda}_{i,k}^* - \bar{\lambda}_{j,k}} = 0 \\ \bar{\boldsymbol{f}}_k = \dfrac{\boldsymbol{f}_k}{\sigma_{x_l^*}} \\ \boldsymbol{u} = \bar{\boldsymbol{V}}^{\mathrm{T}}\boldsymbol{\xi} \end{cases} \tag{11}$$

where $\bar{\lambda}_{i,k}^*\left(i = 1, 2, \cdots, 2n\right)$ are the eigenvalues of $\dfrac{1}{w-1}\bar{\boldsymbol{Y}}_k^{\mathrm{T}}\bar{\boldsymbol{Y}}_k$ in descending order; and $\bar{\boldsymbol{V}}$ contains the corresponding eigenvectors matrix.

Then, the expectation of $\bar{\lambda}_{1,k}$ satisfy:

$$\mathbb{E}\left\{\bar{\lambda}_{1,k}\right\} > \mathbb{E}\left\{\frac{\bar{\boldsymbol{f}}_k^{\mathrm{T}}\bar{\boldsymbol{f}}_k}{w}\right\} + \bar{\lambda}_{n-1,k}^* > \frac{t_{\mathrm{f}}}{w}\mathbb{E}\left\{\bar{\boldsymbol{f}}_k^2\right\} \tag{12}$$

where $t_{\mathrm{f}} \leqslant w$ represents the fault duration in the time window w.

Based on [28], the lower limit of maximum eigenvalue for $\boldsymbol{C}_k$ is:

$$\lambda_{1,k} \geqslant \bar{\lambda}_{1,k} + \min_{1\leqslant j\leqslant 2n}\bar{\lambda}_{j,k}(\boldsymbol{C}_{2,k}) \tag{13}$$

For $\boldsymbol{C}_{2,k}$, incipient fault cases, $\xi_l = 1$. Therefore, by mathematical induction [34], there is:

$$\mathbb{E}\left\{\min_{1\leqslant j\leqslant 2n}\bar{\lambda}_{j,k}(\boldsymbol{C}_{2,k})\right\} = -\sqrt{\frac{t_{\mathrm{f}}(n-1)}{w^2}\mathbb{E}\left\{\bar{\boldsymbol{f}}_k^2\right\}} \tag{14}$$

It should be noted that, owing to the inherent variations in battery characteristics and connection resistances, the voltage standard deviations typically differ

among batteries. Taking into account the need for global fault detectability, the detection threshold δ_3 for incipient VS faults can be appropriately bounded, as:

$$\delta_3 \leqslant \frac{1}{\sigma_{\lambda_1^*}}\left[\frac{t_{\mathrm{f}}}{w}\mathbb{E}\left\{\bar{\boldsymbol{f}}_k^2\right\}-\sqrt{\frac{t_{\mathrm{f}}(n-1)}{w^2}\mathbb{E}\left\{\bar{\boldsymbol{f}}_k^2\right\}}-\mu_{\lambda_1^*}\right] \tag{15}$$

Hence, if the allowable incipient VS fault amplitude f is determined in prior, the detection threshold δ_3 can be obtained by the allowable VS fault amplitude f.

2) Detection Threshold for SC and EC Fault

For the SC fault, denote the fault f at the lth channel $s_{1,l}$, and the measurement vector can be expressed as follows:

$$\boldsymbol{x} = \boldsymbol{A}(\boldsymbol{s}_1 + \boldsymbol{\xi} f) + \boldsymbol{B}\boldsymbol{s}_2 \tag{16}$$

$\bar{\boldsymbol{X}}$ in time window w can be normalized as:

$$\bar{\boldsymbol{X}}_k = (\boldsymbol{X}_k^* + \boldsymbol{f}_k\boldsymbol{\xi}_k^{\mathrm{T}}\boldsymbol{A}^{\mathrm{T}})\boldsymbol{\Sigma}_0^{-1} = \bar{\boldsymbol{Y}}_k + \boldsymbol{f}_k\boldsymbol{\xi}_k^{\mathrm{T}}\bar{\boldsymbol{A}}^{\mathrm{T}} \tag{17}$$

The covariance matrix $\boldsymbol{C}_k$ of $\bar{\boldsymbol{X}}$ can be classified into $\sum_{i=1}^{3}\boldsymbol{C}_{i,k}$, which is formulated as follows:

$$\begin{cases}\boldsymbol{C}_{1,k} = w^{-1}\bar{\boldsymbol{Y}}_k^{\mathrm{T}}\bar{\boldsymbol{Y}}_k \\ \boldsymbol{C}_{2,k} = w^{-1}\bar{\boldsymbol{Y}}_k^{\mathrm{T}}\boldsymbol{f}_k\boldsymbol{\xi}_k^{\mathrm{T}}\bar{\boldsymbol{A}}^{\mathrm{T}} + w^{-1}\bar{\boldsymbol{A}}\boldsymbol{\xi}_k\boldsymbol{f}_k^{\mathrm{T}}\bar{\boldsymbol{Y}}_k \\ \boldsymbol{C}_{3,k} = w^{-1}\bar{\boldsymbol{A}}\boldsymbol{\xi}\boldsymbol{f}_k^{\mathrm{T}}\boldsymbol{f}_k\boldsymbol{\xi}_k^{\mathrm{T}}\bar{\boldsymbol{A}}^{\mathrm{T}}\end{cases} \tag{18}$$

$\mathbb{E}\{D_k\} \geqslant \delta_1$ needs to be guaranteed, so $\mathbb{E}\{\bar{\lambda}_i\} \geqslant \mu_{\bar{\lambda}_i^*} + \delta_1\sigma_{\bar{\lambda}_i^*}$ for $i \in \{1, 2, \cdots, 2n\}$, where δ_1 is the detection threshold. Based on the additivity of matrix trace, there is:

$$\delta_1 \leqslant \frac{\sum_{i=1}^{2n}\mathbb{E}\{\lambda_{i,k}\} - \sum_{i=1}^{2n}\mu_{\bar{\lambda}_i^*}}{\sum_{i=1}^{n-1}\sigma_{\lambda_i}^*} = \frac{\sum_{j=1}^{3}\mathbb{E}\{\mathrm{Tr}(\boldsymbol{C}_{j,k})\} - \sum_{i=1}^{2n}\mu_{\bar{\lambda}_i^*}}{\sum_{i=1}^{2n}\sigma_{\bar{\lambda}_i^*}} \tag{19}$$

$\boldsymbol{C}_{1,k}$ is the normalized covariance matrix. Due to the eigenvalue expectation satisfying (20), for $\boldsymbol{C}_{2,k}$, there is (21); for $\boldsymbol{C}_{3,k}$, there is (22).

$$\mathbb{E}\{\bar{\lambda}_{i,k}\} = \mu_{\bar{\lambda}_{i,k}^*} \ (i = 1, \cdots, 2n) \tag{20}$$

$$\begin{cases}\mathbb{E}\{\mathrm{Tr}(\boldsymbol{C}_{1,k})\} = \sum_{i=1}^{2n}\mu_{\bar{\lambda}_i^*} \\ \mathbb{E}\{\bar{\boldsymbol{Y}}_k^{\mathrm{T}}\boldsymbol{f}_k\} = 0 \\ \mathbb{E}\{\mathrm{Tr}(\boldsymbol{C}_{2,k})\} = 0\end{cases} \tag{21}$$

$$\mathbb{E}\{\mathrm{Tr}(\boldsymbol{C}_{3,k})\} = \frac{\mathbb{E}\{\boldsymbol{f}_k^{\mathrm{T}}\boldsymbol{f}_k \times \mathrm{Tr}(\bar{\boldsymbol{A}}\boldsymbol{\xi}\boldsymbol{\xi}^{\mathrm{T}}\bar{\boldsymbol{A}}^{\mathrm{T}})\}}{w} = \frac{t_{\mathrm{f}}}{w}\mathbb{E}\{f^2\}\bar{\boldsymbol{a}}_l^{\mathrm{T}}\bar{\boldsymbol{a}}_l \tag{22}$$

where $\bar{\boldsymbol{a}}_l$ represents the lth column of $\bar{\boldsymbol{A}}$.

Then, there is:

$$\bar{\boldsymbol{a}}_l^{\mathrm{T}}\bar{\boldsymbol{a}}_l = 2\left(\sigma_{x_l^*}\right)^{-2}, \ \ l = 1, \cdots, 2n \tag{23}$$

To ensure robustness against duty-cycle variations, by combing (19) with (23), the detection threshold can be derived to satisfy:

$$\delta_1 \leqslant \frac{t_{\mathrm{f}}}{w} \times \frac{\mathbb{E}\{f^2\bar{\boldsymbol{a}}_l^{\mathrm{T}}\bar{\boldsymbol{a}}_l\}}{\sum_{i=1}^{2n}\sigma_{\bar{\lambda}_i^*}} = \frac{2t_{\mathrm{f}}}{w} \times \frac{\mathbb{E}\left\{f^2\left(\sigma_{x_l^*}\right)^{-2}\right\}}{\sum_{i=1}^{2n}\sigma_{\bar{\lambda}_i^*}} \tag{24}$$

Similarly, for incipient EC fault, the detection threshold δ_2 should satisfy:

$$\delta_2 \leqslant \frac{t_{\mathrm{f}}}{w} \times \frac{\mathbb{E}\{f^2\bar{\boldsymbol{b}}_l^{\mathrm{T}}\bar{\boldsymbol{b}}_l\}}{\sum_{i=1}^{2n}\sigma_{\bar{\lambda}_i^*}} = \frac{2t_{\mathrm{f}}}{w} \times \frac{\mathbb{E}\left\{f^2\left(\sigma_{x_l^*}\right)^{-2}\right\}}{\sum_{i=1}^{2n}\sigma_{\bar{\lambda}_i^*}} \tag{25}$$

where $\bar{\boldsymbol{b}}_l$ represents the lth column of $\bar{\boldsymbol{B}}$.

D. Fault Localization Analysis

Calculating and analyzing D_k serves as the initial step in the proposed methodology, providing a preliminary assessment of battery safety status with minimal computational intensity. In this subsection, the battery fault will be finally diagnosed. Upon detection of a fault, the specific fault type and its location are further determined by evaluating the contribution of abnormal eigenvalues.

The eigenvectors $\boldsymbol{v}_{m,k}$ corresponding to the covariance matrix $\boldsymbol{C}_k$ of the streaming sample matrix $\bar{\boldsymbol{X}}_k$ satisfy:

$$\boldsymbol{C}_k\boldsymbol{v}_{m,k} = \lambda_{m,k}\boldsymbol{v}_{m,k}, \ \ m = 1, 2, \cdots, 2n \tag{26}$$

where $\boldsymbol{v}_{m,k}$ is the mth column of the eigenvector matrix.

The contribution of the ith row of a covariance matrix to the eigenvalue $\lambda_{m,k}$ can be assessed by the ith entry of the corresponding eigenvector $\boldsymbol{v}_{m,k}$ [35], which is represented $v_{1,k}^{(i)}$. Then, the final fault indicator is designed according to the maximum element of the eigenvector corresponding to the maximum eigenvalue (ECME).

$$\eta_i = v_{1,k}^{(i)}, \ \ i = 1, 2, \cdots, 2n \tag{27}$$

By analyzing the ECME, the fault status of the batteries can be identified, including fault types and fault location. Referencing Fig. 3, the following insights can be derived:

1) In the case of a VS fault, it can be differentiated from the other two electrical faults when the element

η_i is the smallest, indicating that the fault location is at the *i*th sensor;

2) For a SC fault, the fault location is identified as the *i*th cell when the two neighboring elements η_{2i-1} and η_{2i} are the two smallest values;

3) For an EC fault, the fault location is the EC between the *i*th and $(i+1)$th cell when the two neighboring elements η_{2i} and η_{2i+1} are the two smallest values.

The implementation of an interleaved measurement topology enables straightforward discrimination among SC, EC, and VS faults, under the assumption that only one type of battery fault occurs at a single location. A VS fault impacts just one sensor, resulting in a single abnormal value within the ECME, with the index of this abnormal value indicating the fault location. Conversely, both SC and EC faults influence two adjacent sensors, causing two neighboring values in the ECME to be abnormal. Specifically, as illustrated in Fig. 3 and detailed in this subsection, for a SC fault, the smaller number of sensors among the affected neighboring sensors is an odd number; whereas for an EC fault, it is an even number. The location of SC and EC faults can be directly determined, ensuring that the localization logic for the three fault types remains distinct and non-overlapping.

$$\begin{cases} L_1 = (s+1)/2 \\ L_2^{\mathrm{L}} = s/2 \\ L_2^{\mathrm{R}} = s/2+1 \\ L_3 = s \end{cases} \tag{28}$$

where L_1 and L_3 denote the locations of SC and VS faults, respectively; L_2^{L} and L_2^{R} represent the serial numbers of the batteries to the left and right of the connection fault location, respectively; and s signifies the smaller serial number of neighboring anomalous sensors, if there is only one anomalous sensor, s is its serial number.

The diagram of sensors impacted by three types of faults is illustrated in Fig. 4.

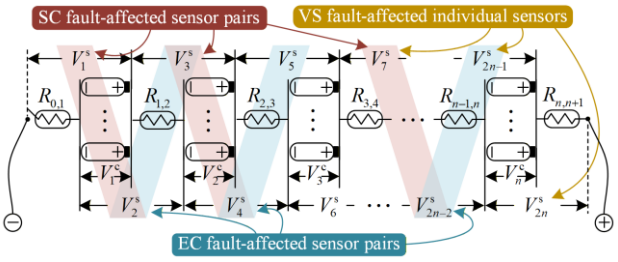

Fig. 4. The diagram of sensors affected by three kinds of faults.

E. Whole Multi-fault Detection and Diagnosis Procedure

The complete multi-fault diagnosis procedure for SC, EC, and VS faults is depicted in Fig. 5, encompassing two primary stages: adaptation and fault diagnosis. During the adaptation phase, the BMS operates without conducting fault diagnosis. This stage typically occurs during the pre-factory fault-free trial operation. The BMS analyzes extensive operational data to derive reference parameters and normalized detection thresholds from the datasets, as detailed in Sections II.A and II.B. Subsequently, in the fault diagnosis step, the BMS continuously monitors the battery system's condition, comparing it against the established fault detection thresholds. Specifically, the BMS first evaluates the battery's safety status by calculating and analyzing D_k, a process referred to as preliminary judgement. If D_k indicates an anomaly, the BMS proceeds to calculate and analyze the ECME for a more in-depth diagnosis of the battery fault. Upon detecting a fault, the BMS identifies the fault type and pinpoints its location using the ECME elements, a step termed further judgement. The specifics of the fault diagnosis process are outlined in Algorithm 1.

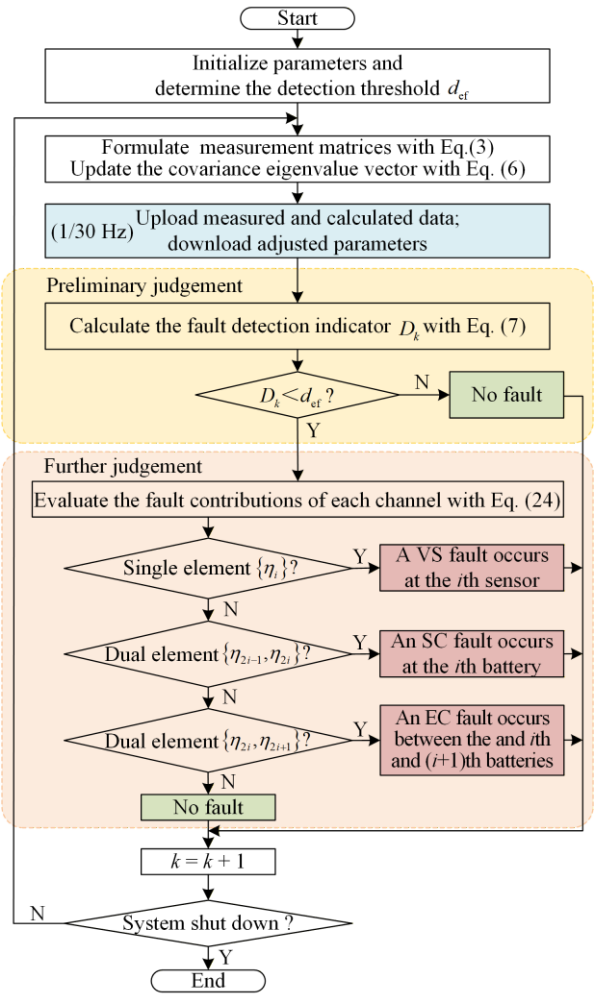

Fig. 5. Flowchart of the multi-fault diagnosis method.

Algorithm 1 Fault Diagnosis Process

Input: A data vector $\boldsymbol{x}$ denoting the measured battery voltage and a data matrix $\boldsymbol{X}$ representing the saved battery voltage within the time window

Output: The vector $\boldsymbol{y}$ signifying the fault status, 0 for fault free, 1 for SC fault, 2 for EC fault at the positive terminal, and 3 for VS fault

// Step 1: construct the raw data matrix
Delete the oldest data of $\boldsymbol{X}$; Insert $\boldsymbol{x}$ into $\boldsymbol{X}$
// Step 2: Calculate the detection indicator $\boldsymbol{D}$
Normalize $\boldsymbol{X}$ and get $\bar{\boldsymbol{X}}$
Find the covariance matrix $\boldsymbol{C}$ of $\bar{\boldsymbol{X}}$
Find the vector of eigenvalues $\boldsymbol{e}$ of $\boldsymbol{C}$
$D = \max(\boldsymbol{e})$
// Step 3: preliminary judgement
If $D > \delta$ then
$\boldsymbol{y} = 0$
Return $\boldsymbol{y}$
End if
// Step 4: further judgement
Find the eigenvector $\boldsymbol{v}$ corresponding to $\max(\boldsymbol{e})$, and $\boldsymbol{E}_i$ is the ith element in $\boldsymbol{v}$
Find the index number $\{i\}$ of the $\boldsymbol{E}_i$ below the mean
If there is only one element $\boldsymbol{E}_i$, then
$\boldsymbol{y}[i] = 3$
Else if there are two elements $\boldsymbol{E}_{2i-1}$ and $\boldsymbol{E}_{2i}$, then
$\boldsymbol{y}[i] = 1$
Else if there are two elements $\boldsymbol{E}_{2i}$ and $\boldsymbol{E}_{2i+1}$, then
$\boldsymbol{y}[i] = 2$
End if
Return $\boldsymbol{y}$

F. Cloud Edge Collaboration

Most battery fault diagnosis methods are executed within the BMS, relying on local data for both operation and optimization. The local computing mode (LCM) enables rapid fault detection and alerting, though data silos significantly hinder both the speed and comprehensiveness of parameter optimization. The cloud computing mode (CCM) addresses this limitation by enabling centralized management of algorithm processes and vast battery datasets. Owing to its robust computing capabilities, expansive storage, and advanced big data algorithms, CCM is gaining widespread adoption in early-stage battery fault diagnosis. However, as the number of ESS surges, CCM faces escalating computational and communication demands, leading to higher server costs. Besides, the inherent unpredictability of network failures undermines its real-time performance.

To tackle the aforementioned problems, a cloud-edge collaborative (CEC) framework for the proposed method has been developed. Within this framework, the BMS functions as an edge device, shouldering the bulk of computational responsibilities. Despite the algorithm's inclusion of computationally demanding operations, these tasks are assigned to the slave module within the BMS. Additionally, the algorithm is divided into two segments, with partial calculations often proving adequate to evaluate battery safety status, thereby diminishing overall computational demands. These optimizations render the algorithm feasible for execution on edge devices. The server, serving as a cloud device, refines the parameters of the fault diagnosis method through battery big data mining, thereby overcoming the issue of information silos. It also gathers operational data from the batteries, enabling remote monitoring and control of the battery systems. Given that specific battery data calculations are handled by the BMSs, communication intensity is minimized, and the expenses associated with server setup or leasing are reduced. A comparison between LCM, CCM, and CEC is illustrated in Fig. 6, while the task distribution within the cloud-edge collaboration is depicted in Fig. 7.

Evaluation	LCM	CCM	CEC
Support complex algorithms		●	●
Big data surport		●	●
Low computational intensity	●		●
Low communication intensity	●		●
Cost saving	●		●
Timely response	●		●

Fig. 6. The comparison of LCM, CCM, and CEC.

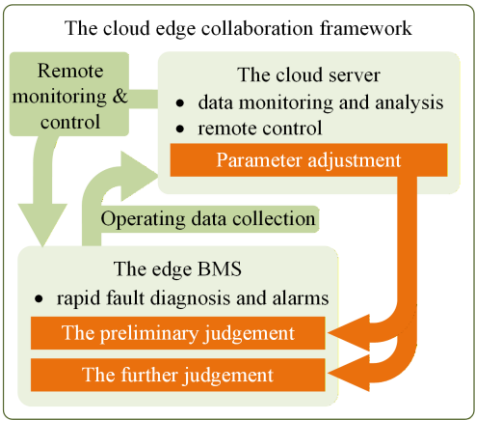

Fig. 7. The tasking for the cloud edge collaboration.

Given the high voltage levels in BSS, BMS typically adopts a master-slave architecture. As an edge device within the cloud-side collaborative framework, the BMS primarily handles data computation for the battery pack. To enhance efficiency, it's often advantageous to distribute computational tasks across multiple devices. Despite the master module in the BMS possessing slightly superior computational capability compared to the slave modules, in large-scale systems comprising one master module and over eight slave modules, the slave modules are more suitable for undertaking computations within the battery pack.

Therefore, the slave module is tasked with monitoring battery voltage, computing D_k and the ECME, and then transmitting these calculation results to the master module. Based on these results, the master module implements protective actions and issues alarms as necessary. The battery array unit serves as the top-tier

component of the BMS, storing data from all batteries across the entire battery system and managing the EC between each battery cluster and the high-voltage busbar. The data transfer module establishes a direct communication pathway with the server, utilizing protocols such as TCP or UDP, via Ethernet, WLAN, or 5G networks. Depending on specific technical needs, it can communicate directly with the BMS or do so indirectly through the energy management system (EMS). The system's structure and communication flow are illustrated in Fig. 8.

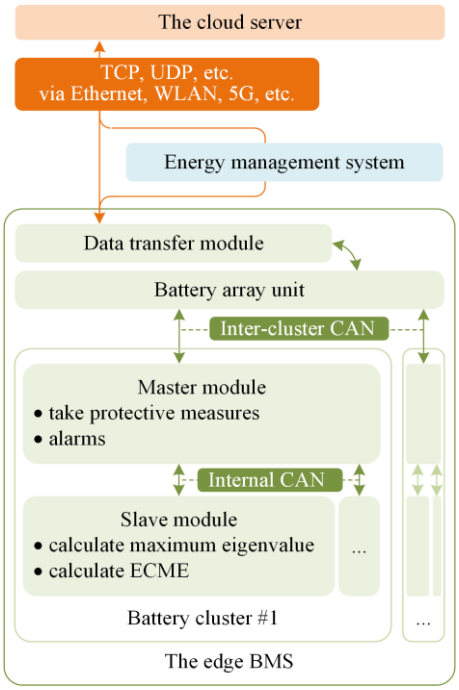

Fig. 8. The system structure and communication of the cloud edge collaboration.

G. The Practical Measurement and Analysis Method

A battery pack typically comprises hundreds of batteries connected in series, often organized into several battery modules, with each module housing dozens of batteries. The optimal solution for fault diagnosis involves voltages across all batteries, generating a comprehensive matrix that encompasses data from all sensors, and then conducting a centralized analysis of battery fault conditions-a method referred to as the original measurement and analysis (ORMA). However, this method reduces the modularity of the modules and compromises the reliability of the BMS.

1) ORMA reduces the modularity of modules. The assembly of battery packs is designed to be highly modular. Typically, a battery pack includes a high-voltage control box and multiple battery modules. Each battery module is independently assembled, incorporating dozens of batteries along with a BMS slave module. Under the ORMA scheme, each battery module needs to be interconnected with neighboring modules via six wires, as depicted in Fig. 9, which drastically erodes module independence and complicates the battery assembly process.

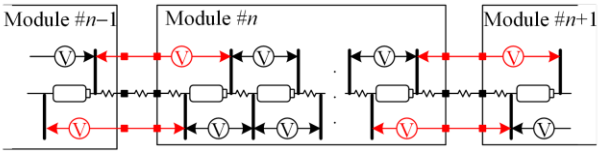

Fig. 9. The circuit topology of the ORMA.

2) ORMA reduces the reliability of BMSs. Battery voltage measurement wires convey minute current signals that are highly susceptible to electromagnetic interference (EMI). Consequently, BMS are typically housed within metal enclosures to shield them from external EMI. However, lengthy metal wires can act as antennas, readily allowing external EMI to penetrate the BMS and thereby diminish its reliability.

To address this issue, an interleaved measurement topology can be employed within each module, as illustrated in Fig. 10, and this approach decouples the measurement matrix and analysis processes among slave modules, a method termed OPMA. It is important to note that OPMA does not adversely affect the diagnosis of SC faults, VS faults, or EC faults within a module, and OPMA offers the benefits of low calculation cost and cloud-side collaboration.

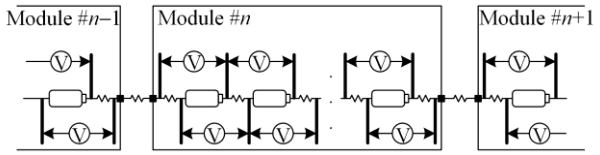

Fig. 10. The circuit topology of the OPMA.

1) OPMA have low calculation cost. The calculation cost of the proposed method primarily lies in determining the eigenvectors of the covariance matrix. QR decomposition, a widely adopted technique for eigenvalues computation, has a time complexity of $O(n^3)$, where n represents the number of batteries [36]. In the OPMA approach, the volume of data processed at any given time is solely dependent on the number of series-connected batteries within each module. Consequently, OPMA theoretically requires M^3 times less processing time than ORMA, where M denotes the number of slave modules in the BMS.

2) OPMA are cloud-side collaboration friendly. Nowadays, cloud servers are extensively utilized in early-stage battery fault diagnosis, thanks to their superior computing capabilities, expansive storage capacity, and advanced big data algorithms. CCM facilitates centralized management of algorithm processes and battery big data, yet it increasingly grapples with burdensome computational demands.

To tackle this challenge, the OPMA approach transitions battery fault diagnosis from CCM to a CEC computing paradigm, where BMS slave modules

undertake detailed calculations, while cloud servers focus on data mining and parameter refinement. The CEC computing mode boasts a streamlined architecture, relieving cloud servers of the need to handle vast, repetitive, and monotonous computational tasks.

H. Computational and Communication Intensity

In this subsection, the computational workload associated with the eigen decomposition-based method is analyzed and the optimization achieved through OPMA is evaluated. The communication intensity, measured by the volume of data transferred per second, is computed while communicational intensity is quantified by the count of basic operations (BOs), namely, addition, subtraction, multiplication, and division.

The eigen decomposition algorithm comprises the computation of the covariance matrix $\boldsymbol{C}_k$ and the symmetric QR algorithm. According to (6), computation of $\boldsymbol{C}_k$ include one matrix multiplication and one pointwise matrix division, and requires $8wn^2+4n^2$ BOs. The symmetric QR algorithm includes householder tridiagonalization as well as eigenpair computation. According to [37], the computation of eigenvalues and eigenpairs require $32n^3/3$ and $72n^3$, respectively. It should be noted that the threshold of D_k has an impact on the computational intensity. Ideally, ECME does not need to be computed when the overall computational intensity is reduced to approximately $32n^3/3+8wn^2$. Moreover, the recursive analysis method reduces the computational intensity of eigenvectors to $16n^2$, compared to that of eigenvalues, which is negligible [38]. Integrating this approach has the potential to further diminish the computational demands of the proposed method, representing a key avenue for our future work.

In real-world applications, the algorithm operates under the OPMA framework within the slave modules of BMS. Typically, a single slave module monitors either 24 or 48 batteries, thereby capping the maximum computational intensity at the battery count level. Computational tasks related to other batteries are handled by the corresponding slave modules. Although OPMA reduces the overall computational intensity, it necessitates additional communication infrastructure to facilitate the transmission of diagnostic outcomes and intermediate data. Considering a 1500 V ESS comprising 480 $LiFePO_4$ batteries (hereafter referred to as System A), and employing the data format and system configuration outlined in Table I, OPMA elevates the load factor of the internal CAN communication (as depicted in Fig. 8) from 12.58% to 28.30%, a level that remains within acceptable limits.

TABLE I
DATA FORMAT AND SYSTEM CONFIGURATION

Type	Item	Value
BESS	Rated total voltage (V)	1500
	Number of clusters	10
Cluster	Number of cells in serial (N)	480
	Number of temperature sensors	480
	CAN communication	CAN 2.0B extended frame 250 kbps
	Maximum communication capacity (frames/s)	1908
	Data transmission frequency (Hz)	1
Internal CAN bus	Battery voltage (Bytes)	2N (960)
	Battery temperature (Bytes)	2N (960)
	Subtotal (Bytes)	4N (1920)
	Fault status (Bytes)	1N (480)
	The fault indicator D_k (Bytes)	2N (960)
	The ECME (Bytes)	2N (960)
	Total (Bytes)	9N (4320)

Servers boast substantial computational capabilities, enabling them to handle complex algorithms with ease. However, algorithms reliant solely on servers often suffer from sluggish response times, attributed to the numerous communication intermediaries involved. More importantly, unlike OPMA, server-based algorithms lack the ability to cap maximum computational intensity, leading to significant communication strain. Ultimately, this escalates the costs associated with constructing or renting server infrastructure. Specifically, the server-based algorithm requires at least about $ecb(32n^3/3+8wn^2)$ BOs, where b, c, e denotes the number of slave modules, battery cluster, and BESSs in the respective parent system, respectively. In system A, inter-cluster communication entails transmitting data from all batteries within this BESS, and battery voltage transmission accounts for 62.89% of the CAN bus CAN load, necessitating a reduction in the transmission of other information, which brings difficulties and pitfalls for system design and operation. While transmission blocking issues with server stem from multiple factors and are thus not elaborated upon in this article, it's worth noting that they can significantly complicate matters.

In the proposed cloud-side collaboration architecture, the cloud server plays a pivotal role in adjusting the diagnostic algorithm's operational parameters. Therefore, it imposes minimal demands on the amount, frequency, and real-time nature of data transmission. In System A, inter-cluster communication at a 1 Hz frequency suffices for transmitting concise information. Transmitting voltage and temperature information at approximately 1/30 Hz meets the cloud server's data monitoring requirements, thereby alleviating communication pressure.

III. EXPERIMENT SETUP

To validate the proposed battery fault diagnosis method, an experimental setup is established, comprising

five 50 Ah LFP square aluminum batteries, an Arbin charge device, and a Jufu temperature chamber, as illustrated in Fig. 11.

Fig. 11. Battery experimental setup.

Experiments are carried out at a constant temperature of 25 ℃, with the urban dynamometer driving schedule (UDDS) selected as the battery test condition. The maximum discharge current of UDDS is scaled to 50 A (1 C), and the initial SOC of batteries are 80%, 83%, 85%, 70%, and 75%, respectively.

The schematic diagram of the battery test circuit is presented in Fig. 12. To simulate an SC fault, switch K_1 is closed to short Battery 2 via a 1 Ω R_{SC}, resulting in a short-circuit current of approximately 0.07 C. An EC fault is emulated by cutting $R_{2,3}$, thereby linking Battery 2 and 3 through the 10 mΩ resistor R_{EC}. For normal connections, resistors $R_{0,1}$, $R_{1,2}$, and $R_{5,6}$ are each set to 3 mΩ. A VS fault is introduced by manipulating sensor data post-battery testing. There are two types of VS faults: excessive error and data sticking. The excessive error is simulated by adding a 20 mV white noise to the sensor data, while data sticking is replicated by maintaining the sensor data at the fault's onset throughout the fault duration. Parameters of faults are outlined in Table II.

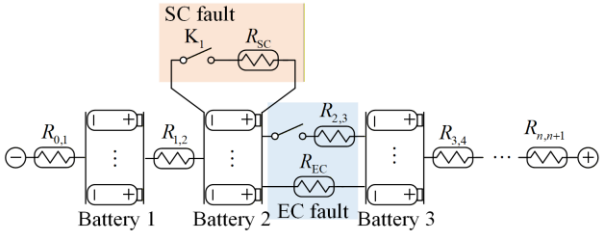

Fig. 12. The equivalent diagram of experiment.

TABLE II
FAULT PARAMETERS

No.	Fault type	Description	Time (s)
1	Short circuit	1 Ω short resistance in Battery 2 (the short-circuit current is approximately 0.07 C)	820–850
2	Electrical connection	10 mΩ connection resistance between Battery 2 & 3	250–280
3	Excessive error	A standard deviation of 20 mV is added to V_3^s	300–400
4	Sensor data sticking	V_3^s sticks	300–400

IV. RESULTS AND DISCUSSIONS

During the tests, the measured $\boldsymbol{V}^s$ data encompass a piece of EC fault data and a piece of SC fault data. The EC fault manifests between 250 s and 280 s, highlighted in blue, while the SC fault occurs from 820 s to 850 s, marked in red. Subsequently, to simulate a VS fault, the data from 400 s to 500 s are manually altered: random values are introduced to mimic excessive error, and the data are fixed to the value at 500 s to replicate the fault of value sticking. The sensor data, D_k and the ECME are depicted in Figs. 13(a), (b), and (c), respectively. There are eight data segments with lower D_k values, identified by gray blocks and numbered 1–8. As illustrated in Fig. 13(b), the additional time required for further fault determination is 184 s, constituting merely 18.4% of the total test duration. It's worth noting that the 184 s includes the time for D_k to approach the threshold and the second response of the SC and EC faults, scenarios that are exceedingly uncommon in practical applications. The battery fault status is ascertained through a deeper analysis of the ECME. The observed phenomena and corresponding diagnostic outcomes for these eight data segments are detailed in Table III.

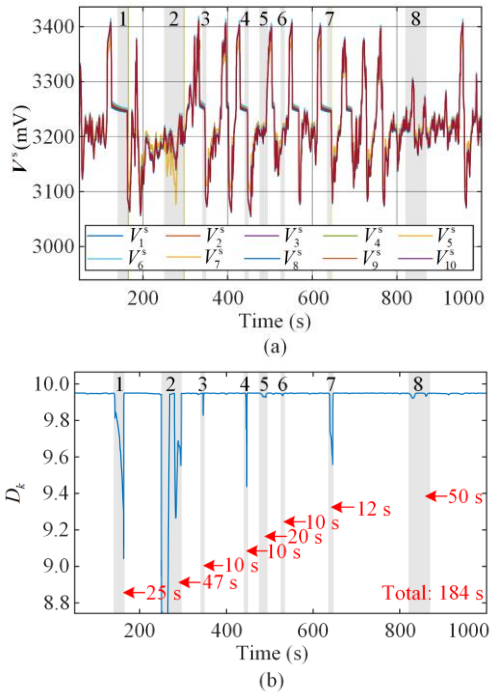

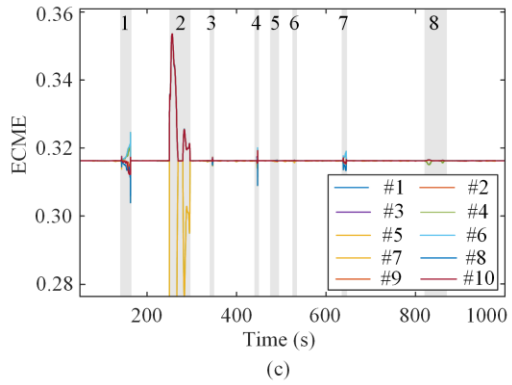

Fig. 13. Experimental data and diagnosis results of the entire experiment. (a) The sensor data. (b) The maximum eigenvalue. (c) Elements in eigenvector.

TABLE III
THE PHENOMENA AND DIAGNOSTIC RESULTS

No.	Min D_k	Description of eigenvector	Diagnosis result
1	9.043	{7, 8, 9, 10} below average	No fault
2	7.956	{4, 5} below average	SC fault at Battery 2, as shown in Section IV.A
3	9.828	{1, 2, 4, 5, 6} below average	No fault
4	9.438	{1, 2, 7, 8, 9, 10} below average	No fault
5	9.927	{3, 4, 5, 9, 10} below average	No fault
6	9.935	{4, 5, 7, 8} below average	No fault
7	9.558	{1, 2, 7, 8, 9, 10} below average	No fault
8	9.921	{3, 4} below average	EC fault at 3rd connection point, as shown in Section IV.B

Determining the magnitude of the maximum eigenvalue serves as the initial step in fault diagnosis. When this eigenvalue exceeds the predetermined threshold, the system is normal and no further calculations are required. If the maximum eigenvalue falls below the threshold, a more detailed analysis of the eigenvector elements becomes necessary. In certain exceptional scenarios, significant current fluctuations may cause a decrease in the maximum eigenvalue, but patterns of elements in the eigenvector do not align with any known fault characteristics. Thus, the diagnostic conclusion remains that no fault is present.

A. Short Circuit Diagnosis

The threshold of D_k for SC fault (d_1) is calculated by fault-free data. Based on (24), the faulty part $f = 6$ mV and $t_f = w$, giving d_1 to be 9.9324, and the calculation process of d_1 is demonstrated in Fig. 14. The detection range represented by d_1 includes a small number of D_k anomalies caused by current mutations, which require ECME for further judgment.

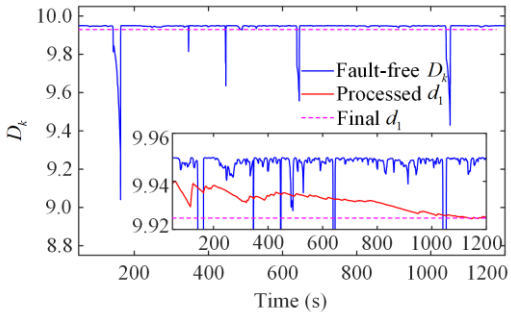

Fig. 14. The calculation process of d_1.

Unlike fault diagnosis, there is no time window for the calculation of d_1. The value at each moment in Fig. 14 is computed from all historical data up to that moment. The d_1 is finally set to the value of the last moment in the threshold setting time. Note that the purpose of Fig. 14 is only to illustrate the calculation process. In practice, it is only necessary to calculate d_1 at the last moment.

The experimental data and diagnosis results of the SC experiment are depicted in Fig. 15. The D_k is displayed in Fig. 15(a), and the ECME is represented in Fig. 15(b). The 1 Ω resistor, used to simulate a fault, is connected to the second battery between 820 s and 850 s, triggering a rapid and discernible shift in the ECME. This change persists for a 20 s interval, which is called as the first response. In the ECME, only the neighboring elements {3, 4} fall below the average, clearly indicating that a SC fault has occurred at Battery 2.

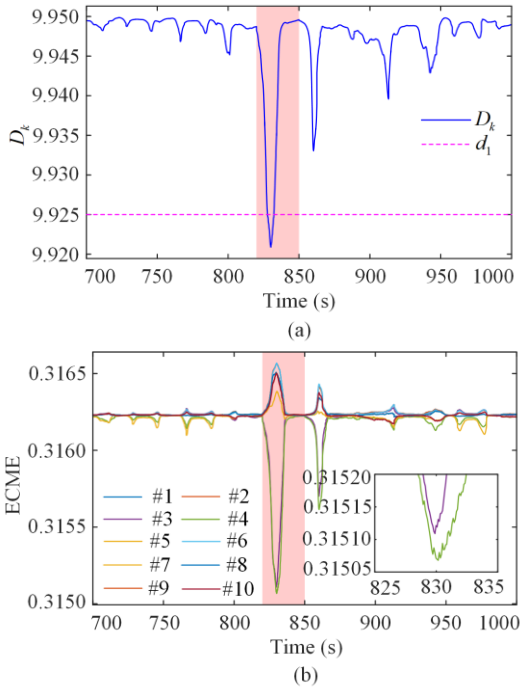

Fig. 15. The ECME of the SC fault. (a) D_k. (b) ECME.

At 840 s, the initial time window elapses. Despite the ongoing SC fault, the ECME reverts to its normal state, a phenomenon we term the advanced recovery.

Subsequently, at 850 s, as the SC fault resolves, the ECME undergoes another transformation with similar regularity, an event referred to as the second response.

B. Electrical Connection Fault Diagnosis

According to (25), the faulty part f = 60 mV and $t_f = w$, giving d_2 to be 8.1929, and the calculation process of d_2 is illustrated in Fig. 16. EC faults have a greater influence on battery data than incipient SC faults. Thus, the detection range represented by d_2 excludes the interference of D_k anomalies caused by sudden current changes.

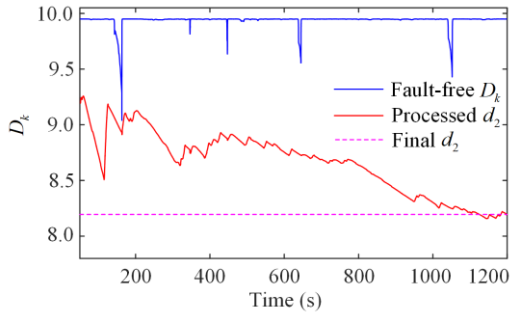

Fig. 16. The calculation process of d_2.

The experimental data and diagnosis from the EC experiment are presented in Fig. 17. Specifically, the D_k is displayed in Fig. 17(a), and the ECME is represented in Fig. 17(b). When there is no fault, the connection resistance stands at 3 mΩ. However, from 250 s to 280 s, this resistance increases to 10 mΩ, triggering the first response. In the ECME, only the neighboring elements {4, 5} fall below the average, clearly signaling an EC fault occurring between Battery 2 and 3.

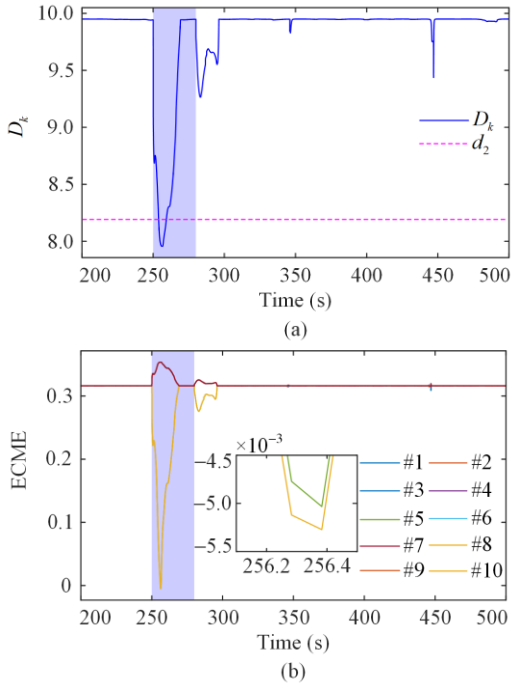

Fig. 17. The ECME of the EC fault. (a) D_k. (b) ECME.

Much like the SC fault scenario, there are also the advanced recovery at 270 s and the second response at 280 s.

C. Excessive Sensor Error Fault Diagnosis

Based on (15), with the faulty part f = 15 mV and $t_f = w$, the calculated d_3 equals 9.8886, and the computation process for d_3 is illustrated in Fig. 18. A few anomalies in D_k resulting from current fluctuations require ECME for further judgment.

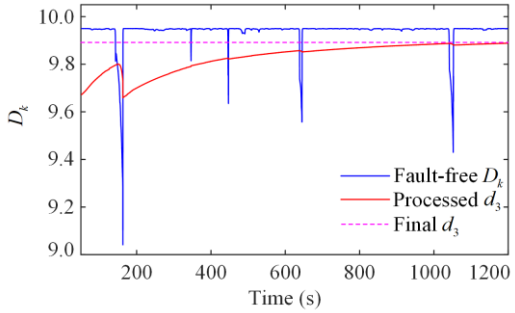

Fig. 18. The calculation process of d_3.

The experimental data and diagnosis outcomes of excessive error in sensor data are depicted in Fig. 19, where the D_k is displayed in Fig. 19(a), and the ECME is represented in Fig. 19(b). The VS faults occur from 300 s to 400 s. Notably, the pronounced ECME response before 300 s in Fig. 19 is attributed to an EC fault. Starting at 300 s, the VS faults induce a significant response in the ECME. Unlike SC and EC faults, the VS fault introduces persistent noise into the sensor data, continuously affecting sensor readings, resulting in the advanced recovery not appearing.

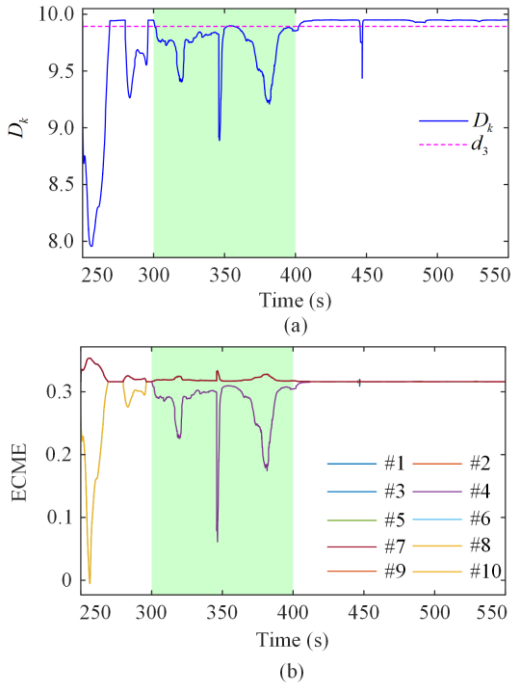

Fig. 19. The ECME of excessive sensor error. (a) D_k. (b) ECME.

In the ECME, only element {3} registers below the average, signifying that the VS fault originates from the third sensor.

D. Sensor Data Sticking Fault Diagnosis

The experimental data and diagnosis results for sensor data sticking are presented in Fig. 20, where the D_k is displayed in Fig. 20(a), and the ECME is represented in Fig. 20(b). The VS faults occur from 300 s to 400 s. Much like the excessive error scenario, sensor sticking exerts a continuous impact; therefore, the advanced recovery does not appear. The difference is that the data sticking causes the readings from the faulty sensor to be entirely inconsistent with those from other sensors, resulting in a constant D_k of 0.

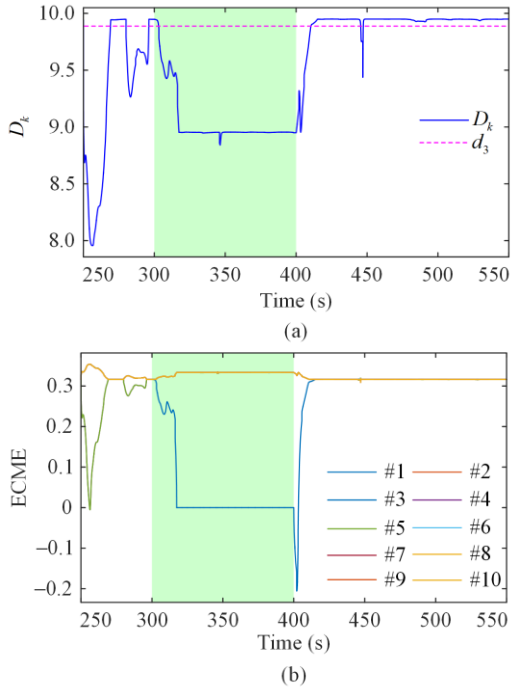

Fig. 20. The ECME of sensor data sticking. (a) D_k. (b) ECME.

In the ECME, only element {3} falls below the average, indicating that the VS fault originates from the third sensor.

E. The First Response, the Advance Recovery, and the Second Response

Interleaved voltages are monitored within a designated time window. When a fault arises, the faulty channel exhibits a distinct change pattern compared to other channels, triggering an anomaly in the ECME, known as the first response.

Throughout this window, faulty data is continuously incorporated into processing, ensuring the anomaly persists until the window concludes. The process by which this anomaly gradually diminishes is termed the advanced recovery. This feature updates the fault detection status dynamically, ensuring the fault diagnosis process remains uninterrupted. It has a high value of use in the design of other battery fault diagnosis methods.

Similarly, fault recovery, just as fault occurrence, induces an anomaly that lasts for the duration of the window, referred to as the second response. For experimental safety and equipment durability, battery fault simulations typically include fault recovery. However, in practical applications, batteries rarely recover from internal SC faults and EC faults, making the second drop exceptionally uncommon.

F. Robustness Analysis

The proposed method's robustness primarily stems from its insensitivity to coordinated variations in battery responses induced by current fluctuations. To verify this, two kinds of noise are introduced into the battery measurement data: DC bias noise and common-mode white Gaussian noise. DC bias noise simulates measurement errors inherent in BMSs, while common-mode white Gaussian noise represents value fluctuations due to EMI. Detailed noise parameters are outlined in Table IV. The experimental data and diagnostic results for each interference type are presented in Figs. 21(a) and (b).

TABLE IV
THE NOISE PARAMETERS

No.	Noise parameters
1	DC bias noise for each channel (mV): [4, 6, 4, 6, 4, 6, 4, 6, 4, 6]
2	Common-mode white Gaussian noise N (0, 5 mV)

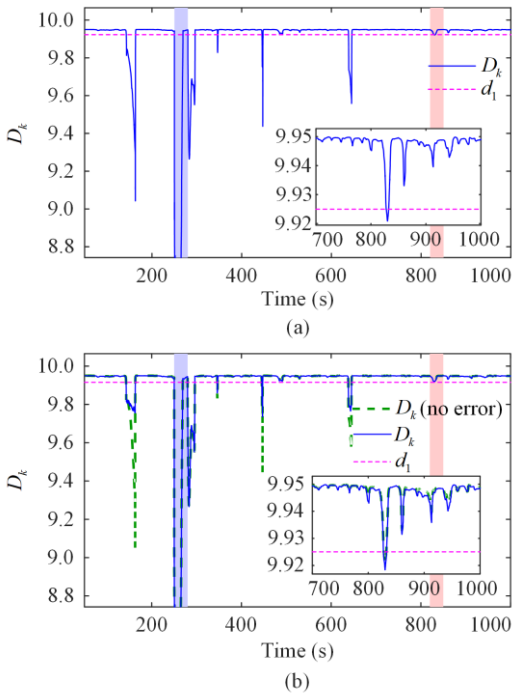

Fig. 21. The diagnostic data with the introduction of Gaussian white noise. (a) DC bias noise. (b) common-mode white Gaussian noise.

DC bias noise exerts no influence on fault diagnosis. The common-mode white Gaussian noise yields dual effects: in regions where D_k exhibits notable anomalous, the common-mode characteristic mitigates inconsistent battery voltage variations, thus having a positive

impact on D_k; conversely, in areas where D_k is normal, it intensifies battery voltage fluctuations, resulting in a negative effect. The diagnosis of SC and EC faults remains accurate, with no instances of misdiagnosis or false alarms observed despite the introduction of these two kinds of noise.

G. Limitations of the Proposed Method

The proposed approach involves matrix eigen-decomposition, making its general implementation more computationally demanding compared to the correlation coefficient method. For the proposed method, there is still room for optimization. Reference [39] introduces a recursive eigen-decomposition method leveraging the rank-one transformation of temporal matrices. This method renders the computation of eigenvalues virtually negligible and reduces eigenvector calculation to just $4m^2$ BOs, thereby substantially lowering overall computational complexity. Moving forward, we aim to further refine the computational intensity of the proposed algorithms and improve their adaptability in edge devices.

H. The Fault Diagnosis Performance

This subsection evaluates the fault diagnosis performance of the proposed method alongside comparative approaches in [15] and [40] using two key metrics: the fault detection rate (FDR) and the false alarm rate (FAR), defined as follows:

$$\begin{cases} R_{\mathrm{FDR}} = N_{\mathrm{D}} / N_{\mathrm{T}} \times 100\% \\ R_{\mathrm{FAR}} = N_{\mathrm{F}} / N_{\mathrm{N}} \times 100\% \end{cases} \tag{29}$$

where N_{D} denotes the detected sample number in faulty time; N_{T} represents the total faulty sample number; N_{F} signifies the false alarm sample number; and N_{N} is the total fault-free sample number. For the SC and EC faults, the value of N_{T} is the time window width.

The compared methods are assessed using battery data from this study, with fault parameters detailed in Table II, where the SC current is 0.064 C and the EC resistance is 10 mΩ. The detection outcomes of these methods are depicted in Fig. 22, while the FDR and FAR values are presented in Table V. The proposed method employs d_1 as a unified threshold. The compared methods utilize 0.9 as the judgement threshold, and detect the EC fault but not the SC fault. Besides, they generate two false alarms.

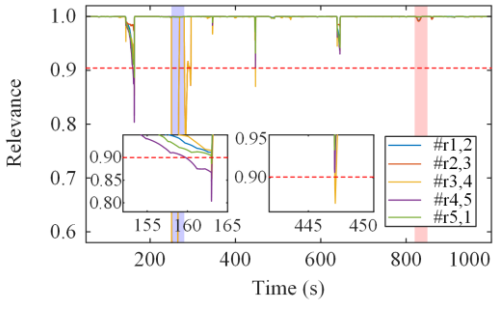

Fig. 22. The detection result of the compared methods.

TABLE V
THE FDR AND FAR OF THE PROPOSED AND COMPARED METHODS

Items	The proposed method	[15] and [40]
SC fault detected	●	○
EC fault detected	●	●
False alarm times	0	2
FDR of SC fault	30 %	0
FDR of EC fault	95.2%	94.7 %
FAR	0	0.4 %

Note: ● indicates the function is implemented; ○ indicates the function is not implemented.

Increasing the threshold to a level that enables detection of the SC fault results in a higher number of false alarms, primarily because the method lacks a mechanism to attenuate non-fault components. To enhance the detectability of weak fault features, the proposed method incorporates pattern matching to filter out non-fault elements during subsequent assessments. A definitive diagnosis requires that the ECME strictly adhere to the condition indicative of a single fault occurrence. Taking the SC fault as an example, the fault-specific ECME pattern is depicted in Fig. 23. Any deviation from this pattern should not be interpreted as a fault condition. For example, in a battery module comprising several dozen cells, incipient faults are infrequent and unlikely to manifest simultaneously across multiple cells. If approximately half of the ECME elements fall below the average, as illustrated in Fig. 24(a); or if the ECME indicates a pattern suggesting two or three simultaneous faults, as shown in Fig. 24(b), these scenarios should not be classified as fault statuses. Most cases of non-faulty anomalous D_k can be filtered out by this pattern determination of ECME in further judgement, thereby allowing for a lower detection threshold for D_k to identify incipient faults with weak features.

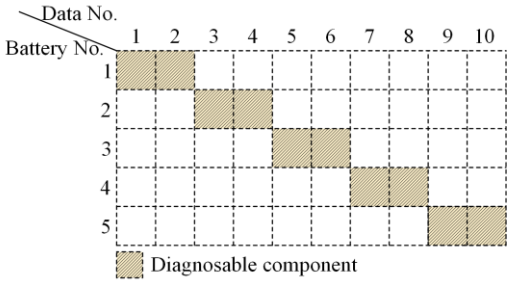

Fig. 23. The faulty pattern of ECME for the SC fault.

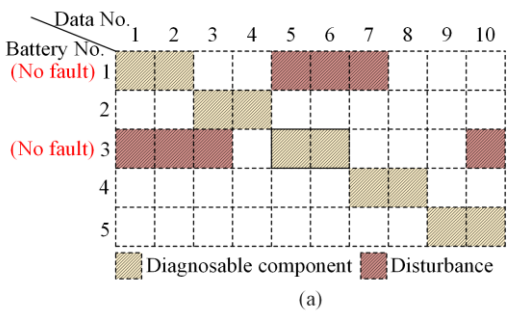

(a)

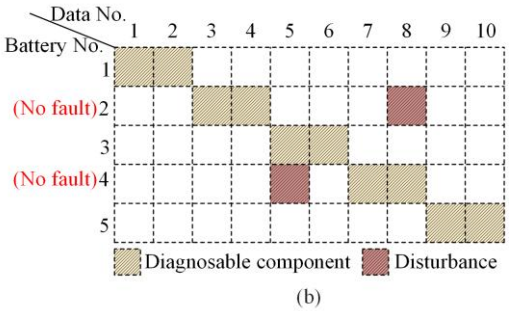

Fig. 24. The fault-free pattern of ECME for the SC fault. (a) Type 1. (b) Type 2.

V. Conclusion

In this study, an eigen decomposition-based approach for battery fault diagnosis is proposed, which realizes the online diagnosis of SC, EC, and VS faults. The primary strengths of this method are outlined below.

1) Excellent fault diagnosis ability. The proposed method achieves accurate diagnosis without misclassification, successfully identifying SC faults at 0.064 C, EC faults with resistances as low as 10 mΩ, and VS faults at 20 mV. Each fault type induces pronounced anomalies during feature extraction. Notably, connection resistances below 10 mΩ are generally not deemed fault-related, and the 20 mV threshold for VS faults is much lower than typical battery inconsistency thresholds.

2) Easy implementation. The proposed method imposes no special requirements on battery VS and does not complicate circuit design, even when sensor redundancy is incorporated.

3) High robustness. Eigenvector feature matching analysis is highly responsive to inconsistent voltage variations but relatively insensitive to voltage fluctuations induced by sudden current changes. Therefore, the proposed method has good robustness under high-current conditions.

4) Cloud-side collaboration friendly. The proposed method operates within BMS slave modules, while cloud servers leverage big data algorithms to extract fault features from battery operational data, enabling dynamic optimization of operational parameters and decision thresholds, achieving cloud-side cooperation.

5) Tolerance for sensor faults. Sensor redundancy enhances the method's tolerance to sensor malfunctions, thereby improving the overall reliability of the BMS.

Future research will concentrate on developing computational optimization techniques, exploring big data-driven methods for battery fault feature extraction, and advancing multi-fault diagnosis strategies for multi-cluster energy storage systems.

Acknowledgment

Not applicable.

Authors' Contributions

Hanxiao Liu: conceptualization, data curation, formal analysis, methodology, software, validation, visualization, writing original draft, writing review, and editing. Luan Zhang: conceptualization, software, and validation. Bin Duan: conceptualization, resources, and supervision. Liwei Li: funding acquisition, project administration, resources, and supervision. All authors read and approved the final manuscript.

Funding

This work is supported in part by the National Natural Science Foundation of China (No. 62133007) and Shandong Provincial Key Research and Development Program (No. 2024CXPT052).

Availability of Data and Materials

Not applicable.

Declarations

Competing interests: The authors declare that they have no known competing financial interests or personal relationships that could have appeared to influence the work reported in this article.

Authors' Information

Hanxiao Liu received the M.S. degree in electrical engineering from Qingdao University, Qingdao, in 2020. Since 2021, he has been a doctoral student at the School of Control Science and Engineering, Shandong University. His research interests include battery management systems and battery fault diagnosis technologies.

Luan Zhang received the B.S. degree in aircraft power engineering from Nanjing University of Aeronautics and Astronautics, Nanjing, in 2020. Since 2022, he has been a master student at the School of Control Science and Engineering in Shandong University. His research interests include battery modeling and fault diagnosis technologies.

Bin Duan received the B.S. degree in automation and the Ph.D. degree in control theory and control engineering from Shandong University, Jinan, China, in 2005 and 2010, respectively. He is currently a professor with the School of Control Science and Engineering, Shandong University. His current research interests include power electronics, battery technology, and modeling and optimal control of complex nonlinear systems.

Liwei Li received the Ph.D. degree in mechanical and electronic engineering from Dalian University of Technology, Dalian, in 2007. He has been a professor at the School of Control Science and Engineering in Shandong University. His research interests include the development of electronic control systems for new energy vehicles, the energy management and collaborative

control of energy storage systems, the electrification and automation "of rail transit, and the intelligent monitoring and condition maintenance of power systems.

REFERENCES

[1] L. Wang, L. Xie, and Y. Yang *et al.*, "Distributed online voltage control with fast PV power fluctuations and imperfect communication," *IEEE Transactions on Smart Grid*, vol. 14, no. 5, pp. 3681-3695, Sep. 2023.

[2] L. Li, Y. Zhao, and Z. Tian *et al.*, "Analytics based energy loss optimization for lithium-ion energy storage system clusters with online fault-tolerance functionality," *Journal of Energy Storage*, vol. 110, Feb. 2025.

[3] W. Liu, M. Xia, and C. Liang, "Real-time simulation and control of a large capacity battery energy storage system directly connecting to a high-voltage grid without a transformer," *Power System Protection and Control*, vol. 52, no. 14, pp. 154-166, Jul. 2024. (in Chinese)

[4] X. Hu, C. Zou, and C. Zhang *et al.*, "Technological developments in batteries: a survey of principal roles, types, and management needs," *IEEE Power & Energy Magazine*, vol. 15, no. 5, pp. 20-31, Sep. 2017.

[5] J. Ren, J. Ma, and H. Wang *et al.*, "A comprehensive review on research methods for lithium-ion battery of state of health estimation and end of life prediction: methods, properties, and prospects," *Protection and Control of Modern Power Systems*, vol. 10, no. 3, pp. 146-165, May 2025.

[6] F. Peng, S. Jiang, and Y. Zhao *et al.*, "Soft short-circuit fault diagnosis for vehicular battery packs with interpretable full-dimensional statistical analytics," *IEEE Transactions on Power Electronics*, vol. 39, no. 9, pp. 11650-11664, Sep. 2024.

[7] H. Chen, Z. Tao, and Y. Zhu *et al.*, "Research on health status and remaining useful life prediction technology for retired lithium-ion power batteries," *Power System Protection and Control*, vol. 53, no. 7, pp. 174-187, Apr. 2025. (in Chinese)

[8] H. Dai, B. Jiang, and X. Hu *et al.*, "Advanced battery management strategies for a sustainable energy future: multilayer design concepts and research trends," *Renewable & Sustainable Energy Reviews*, vol. 138, Mar. 2021.

[9] H. Rahimi-Eichi, U. Ojha, and F. Baronti *et al.*, "Battery management system: an overview of its application in the smart grid and electric vehicles," *IEEE Industrial Electronics Magazine*, vol. 7, no. 2, pp. 4-16, Jun. 2013.

[10] Z. Li, Y. Yang, and L. Li *et al.*, "A weighted Pearson correlation coefficient based multi-fault comprehensive diagnosis for battery circuits," *Journal of Energy Storage*, vol. 60, Apr. 2023.

[11] H. Liu, L. Zhang, and L. Li, "Progress on the fault diagnosis approach for lithium-ion battery systems: Advances, challenges, and prospects," *Protection and Control of Modern Power Systems*, vol. 9, no. 5, pp. 16-41, Sep. 2024.

[12] D. Wang, Y. Yang, and T. Gu, "A hierarchical adaptive extended Kalman filter algorithm for lithium-ion battery state of charge estimation," *Journal of Energy Storage*, vol. 62, Jun. 2023.

[13] H. Liu, L. Li, and B. Duan *et al.*, "Multi-fault detection and diagnosis method for battery packs based on statistical analysis," *Energy*, vol. 293, Apr. 2024.

[14] Z. Liu and H. He, "Sensor fault detection and isolation for a lithium-ion battery pack in electric vehicles using adaptive extended Kalman filter," *Applied Energy*, vol. 185, pp. 2033-2044, Jan. 2017.

[15] Y. Kang, B. Duan, and Z. Zhou *et al.*, "Online multi-fault detection and diagnosis for battery packs in electric vehicles," *Applied Energy*, vol. 259, Feb. 2020.

[16] Y. Xu, X. Ge, and W. Shen *et al.*, "A soft short-circuit diagnosis method for Lithium-ion battery packs in electric vehicles," *IEEE Transactions on Power Electronics*, vol. 37, no. 7, pp. 8572-8581, Jul. 2022.

[17] J. Hu, H. He, and Z. Wei *et al.*, "Disturbance-immune and aging-robust internal short circuit diagnostic for Lithium-ion battery," *IEEE Transactions on Industrial Electronics*, vol. 69, no. 2, pp. 1988-1999, Feb. 2022.

[18] H. Yuan, N. Cui, and C. Li *et al.*, "Early stage internal short circuit fault diagnosis for lithium-ion batteries based on local-outlier detection," *Journal of Energy Storage*, vol. 57, Jan. 2023.

[19] C. Zhang, L. Tu, and Z. Yang *et al.*, "A CMMOG-based lithium-battery SOH estimation method using multi-task learning framework," *Journal of Energy Storage*, vol. 107, Jan. 2025.

[20] C. Zhang, L. Luo, and Z. Yang *et al.*, "Flexible method for estimating the state of health of lithium-ion batteries using partial charging segments," *Energy*, vol. 295, May 2024.

[21] X. Ding, Z. Cui, and H. Yuan *et al.*, "Diagnosis of connection fault for parallel-connected lithium-ion batteries based on long short-term memory networks," *Journal of Energy Storage*, vol. 55, Nov. 2022.

[22] H. He, Z. Liu, and Y. Hua, "Adaptive extended Kalman filter based fault detection and isolation for a Lithium-ion battery pack," in *7th International Conference on Applied Energy*, Abu Dhabi, UAE, Aug. 2015, pp. 1950-1955.

[23] T. Lin, Z. Chen, and C. Zheng *et al.*, "Fault diagnosis of lithium-ion battery pack based on hybrid system and dual extended Kalman filter algorithm," *IEEE Transactions on Transportation Electrification*, vol. 7, no. 1, pp. 26-36, Mar. 2021.

[24] Q. Yu, L. Dai, and R. Xiong *et al.*, "Current sensor fault diagnosis method based on an improved equivalent circuit battery model," *Applied Energy*, vol. 310, Mar. 2022.

[25] D. Shen, D. Yang, and C. Lü *et al.*, "Multi-sensor multi-mode fault diagnosis for lithium-ion battery packs with time series and discriminative features," *Energy*, vol. 290, Mar. 2024.

[26] Y. Xu, X. Ge, and W. Shen, "A novel set-valued sensor fault diagnosis method for Lithium-ion battery packs in electric vehicles," *IEEE Transactions on Vehicular Technology*, vol. 72, no. 7, pp. 8661-8671, Jul. 2023.

[27] C. Zhang, S. Zhao, and Z. Yang *et al.*, "A multi-fault diagnosis method for lithium-ion battery pack using curvilinear Manhattan distance evaluation and voltage

difference analysis," *Journal of Energy Storage*, vol. 67, Sep. 2023.
[28] Z. Chen, C. Zheng, and T. Lin *et al.*, "Multi fault diagnosis of Li-ion battery pack based on hybrid system," *IEEE Transactions on Transportation Electrification*, vol. 8, no. 2, pp. 1769-1784, Jun. 2022.
[29] T. Lin, Z. Chen, and S. Zhou, "Voltage-correlation based multi-fault diagnosis of lithium-ion battery packs considering inconsistency," *Journal of Cleaner Production*, vol. 336, Feb. 2022.
[30] C. Xu, L. Li, and Y. Xu *et al.*, "A vehicle-cloud collaborative method for multi-type fault diagnosis of Lithium-ion batteries," *eTransportation*, vol. 12, May 2022.
[31] Y. Cheng, M. D'Arpino, and G. Rizzoni, "Optimal sensor placement for multi fault detection and isolation in lithium-ion battery pack," *IEEE Transactions on Transportation Electrification*, vol. 8, no. 4, pp. 4687-4707, Dec. 2022.
[32] X. Lai, C. Jin, and W. Yi *et al.*, "Mechanism, modeling, detection, and prevention of the internal short circuit in lithium-ion batteries: recent advances and perspectives," *Energy Storage Materials*, vol. 35, pp. 470-499, Mar. 2021.
[33] N. J. Stor, I. Slapnicar, and J. L. Barlow, "Forward stable eigenvalue decomposition of rank-one modifications of diagonal matrices," *Linear Algebra and its Applications*, vol. 487, pp. 301-315, Dec. 2015.
[34] D. Liu, J. Shang, and M. Chen, "Principal component analysis-based ensemble detector for incipient faults in dynamic processes," *IEEE Transactions on Industrial Informatics*, vol. 17, no. 8, pp. 5391-5401, Aug. 2021.
[35] X. Shi, R. Qiu, and Z. Ling *et al.*, "Spatio-temporal correlation analysis of online monitoring data for anomaly detection and location in distribution networks," *IEEE Transactions on Smart Grid*, vol. 11, no. 2, pp. 995-1006, Mar. 2020.
[36] D. Watkins, "Eigenvalues and eigenvectors I," in *Fundamentals of Matrix Computations*, 2nd ed., New York, USA: John Wiley & Sons, 2002, pp. 356-371.
[37] G. Golub and C. Loan, "Orthogonalization and least squares," in *Matrix Computations*, 4nd ed., Baltimore, USA: Johns Hopkins University Press, 2013, pp. 246-259.
[38] J. R. Bunch, C. P. Nielsen, and D. C. Sorensen, "Rank-one modification of the symmetric eigenproblem," *Numerische Mathematik*, vol. 31, no. 1, pp. 31-48, Jan. 1978.
[39] J. Shang, M. Chen, and H. Ji *et al.*, "Recursive transformed component statistical analysis for incipient fault detection," *Automatica*, vol. 80, pp. 313-327, Jun. 2017.
[40] B. Xia, Y. Shang, and N. Truong *et al.*, "A correlation based fault detection method for short circuits in battery packs," *Journal of Power Sources*, vol. 337, pp. 1-10, Jan. 2017.